Crystalline and Electronic Structures of the Al(1+ x)V2Sn(2-x) (x = 0.19) Intermetallic Compound

Pascal Boulet, Marie-Cécile de Weerd, Emilie Gaudry, Sašo Šturm, Jaafar Ghanbaja, Sylvie Migot, Emmanuelle de Clermont Gallerande, Mostafa Oulfarsi, Jean-Marie Dubois, Vincent Fournée, et al.

Crystalline and electronic structures of the new $Al_{1+x}V_2Sn_{2-x}$ (x = 0.19) intermetallic compound

P. Boulet[1,3], M.-C. de Weerd[1,3], E. Gaudry[1,3], S. Sturm[2,3], J. Ghanbaja[1,3], S. Migot[1,3], E. de Clermont Gallerande[1], M. Oulfarsi[1], J.-M. Dubois[1-3], V. Fournée[1,3] and J. Ledieu[*1,3]

[1]*Institut Jean Lamour, UMR 7198 CNRS- Université de Lorraine, Nancy, France.*

[2]*Jožef Stefan Institute, Department for Nanostructured Materials, Ljubljana, Slovenia.*

[3]*International Associated Laboratory PACS$_2$, CNRS and Université de Lorraine, Nancy France -JSI, Ljubljana, Slovenia.*

e-mail: julian.ledieu@univ-lorraine.fr

Abstract

A new ternary phase with a composition $Al_{1+x}V_2Sn_{2-x}$ (x=0.19) has been found during the investigation of the Al-V-Sn ternary system. Single crystal X-ray diffraction measurements reveal that this ternary phase crystallizes with an orthorhombic structure with a = 5.5931(1) Å, b = 18.8017(5) Å and c = 6.7005(2) Å (Space group Cmce). This compound is thus isostructural to the GaV_2Sn_2 structure type, showing a layered structure composed of vanadium clusters band formed with pentagonal faces intercalated by tin atoms layer. High resolution transmission electron microscopy measurements confirm the orthorhombic structure. Regarding lattice perfection, no dislocation could be identified within the probed $Al_{1.19}V_2Sn_{1.81}$ single crystal lamella. *Ab initio* calculations reveal a reduction of the density of states at the Fermi level, which could be attributed to both a Hume Rothery effect combined with strong *spd* hybridization.

1. INTRODUCTION

As highlighted recently by Dshemuchadse *et al.*[1], ternary compounds are known in only 6% of the theoretically possible ternary intermetallic systems. This gives an idea on how unexplored many systems remain. When experimentally searching for new alloys and intermetallic compounds, several approaches may be considered ranging from random mixing of elements to strategically driven explorations of phase diagrams. Derived from the extensive works performed on quasicrystalline systems, the Push-Pull alloy (PPA) concept has emerged as one route potentially leading to the identification of

new structurally complex ternary intermetallic compounds[2]. For a $A_xB_yC_z$ system, the PPA terminology refers to attractive interactions between constituents in A-B and A-C binary systems (Pull) and to repulsive one between B and C elements (Push), often forming no binary compound or being immiscible. Alternatively, the PPA notion can be understood as a system where the formation enthalpies of pairs of atoms present comparatively large differences. This concept, which is verified so far for most Al-based quasicrystals and for several complex intermetallic compounds[3,4], has already led to the successful identification of new ternary compounds, albeit not complex, in the Al-Au-Ir and Al-Cr-Sc systems.[5,6] The latter intermetallics are thought to be stabilised by a Hume-Rothery mechanism like most quasicrystals. For a given structure, this mechanism, based on a Fermi surface-Brillouin zone interaction, implies a precise electron per atom ratio (e/a), which is only reached for specific stoichiometries, provided that the differences in atomic radii and electronegativities are small (smaller than ~15%). The lowering of the electronic energy can have an effect on the stability only if these 2 conditions are satisfied. This is how benefiting from this electronic stabilisation, Tsai *et al.* revealed the existence of new aperiodic phases by replacing elements of the same column in the Periodic Table, i.e. proceeding to an isoelectronic substitution by preserving constant the e/a ratio.[7,8] To increase the probability of discovering ternary quasicrystalline or approximant phases, these examples demonstrate how the PPA concept could be used in selecting ternary systems while other factors, including Hume-Rothery rules, could help in defining compositional regions of interest within a given phase diagram.

Inspired by the above results and following a careful inspection of binary phase diagrams, we have focussed our attention on the Al-V-Sn system. To our knowledge, there is no report in literature on this selected phase diagram. The PPA criteria are satisfied, as several compounds exist within the Al-V and V-Sn systems while Al and Sn are immiscible. Using conventional characterisation techniques, a dozen of samples of various compositions have been analysed as-cast and after post annealing treatments. Here, we will report on the only ternary phase identified so far within the Al-V-Sn phase diagram. In Section 2, we will describe the experimental and calculation details, including the sample preparation. The crystallographic and electronic structures of the

$Al_{1+x}V_2Sn_{2-x}$ intermetallic will be presented in Section 3 along with the bulk charge distribution before we conclude.

2. EXPERIMENTAL AND CALCULATION DETAILS

2.1 Sample preparation. Based on the electron valence ratios of the pure elements[9], a nominal composition of $Al_{65}V_{30}Sn_5$ was initially selected. This composition leads to an e/a ratio close to those found for stable Mackay icosahedron Al-rich quasicrystalline phases (here e/a=2.2).[9,10] The polycrystalline ingots were obtained by arc-melting stoichiometric amounts of the constituent elements under an atmosphere of high purity argon on a water-cooled copper hearth, using a Ti-Zr alloy as an oxygen getter. The materials were used in the form of ingots using 5N aluminium shot, 2N7 vanadium pieces and 4N tin balls. In order to ensure homogeneity, the arc-melted button was turned over and remelted several times, with weight losses lower than 0.2%. As a preliminary heat treatment, the arc-melted button was wrapped in tantalum foil, sealed in a quartz tube pre-evacuated and refilled with 500mbar He+10%H_2 and heated at 700°C for 5 days. The characterisation of the resulting phases led to the identification of a new ternary $Al_{20}V_{40}Sn_{40}$ compound. Because this ternary phase is in equilibrium with pure Sn, a tin flux single crystal growth method has been chosen to improve the quality of $Al_{20}V_{40}Sn_{40}$ crystallites. Protected with 500mbar He+10%H_2, a button of composition $Al_{20}V_{40}Sn_{40}$ was heated in a tin flux at 1035°C and then cooled down to 788°C at a speed of 0.3°C/min. The excess of Sn has been removed by gravitation and by placing the specimen in an HCl solution.

2.2 Experimental techniques. The single crystal X-ray diffraction (XRD) data were collected on a Bruker Kappa Apex II diffractometer equipped with a mirror monochromator and a Mo Kα IμS (λ = 0.71073 Å) X-ray source. The Apex2 program package was used for the cell refinements and data reductions. The structure was solved by using direct methods and refined with the *SHELXL-2014* program.[11] Semi-empirical absorption correction (SADABS) was applied to the data.

For detailed (scanning) transmission electron microscopy (TEM/STEM) studies of the newly discovered ternary phase ($Al_{1.19}V_2Sn_{1.81}$), TEM specimens were prepared by Focused Ion Beam (FIB) scanning electron microscopy (FEI, Helios Nanolab 600i)

using Ga ions, resulting in electron-transparent lamellas, which were cut perpendicularly to the [100] and [001] directions, respectively. As it will be shown below, Ga ions have been implanted within the lamellae. The estimated thickness of the latter in the imaging region was around 200 Å, with an amorphous surface layer of approximately 15 Å thickness, which was further passivated when exposed to the ambient conditions during specimen transportation. Based on previous studies of Al-based compounds upon oxidation[12], it is assumed that this so-formed stable oxide layer is protecting the inner crystalline part of the specimen against further degradation. As a result, the contrast of the atomically resolved experimental STEM images was not significantly influenced by the formation of the above described passivated layer, as the signal-to-noise-ratio, which was kept at relatively high values is predominately controlled by the crystalline specimen section, typically orientated in the low-indexed crystallographic orientation.

The investigations of composition and atomic resolution STEM imaging was performed by an aberration-corrected TEM (JEOL JEM-ARM200F), using the cold field emission source, equipped with energy Dispersive x-ray Spectroscopy (EDX) system (Centurio 100 mm^2, JEOL). The probe size for Scanning TEM (STEM) imaging was set to 1 Å, with a current of 20 pA and the convergence semi-angle of 24 mrad. STEM images were acquired in a so-called Bright Field (BF) and a High-Angle Annular Dark-Field (HAADF) mode, respectively. The collection semi angle for a HAADF detector was set between 45-180 mrad. The EDX spectrum images were performed with a probe size of 3 Å, under continuous scanning mode with a pixel dwell time of 100 micro seconds and by using a probe current of 30 pA/cm^2. For quantitative image analysis, we performed HAADF-STEM image simulations based on the given experimental electron-optical parameters and the refined crystal structure using an open-source software, QSTEM.[13] Poisson noise was added to the calculated images to mimic realistic conditions during experimental image acquisition.

2.3 Computational details. Calculations based on the Density Functional Theory (DFT) were performed with the Vienna *ab initio* Simulation Package (VASP).[14-17] The interactions between the valence electrons and the ionic core is described using the projector-augmented wave (PAW) method and the calculations are performed with the

generalized gradient approximation (GGA-PBE).[18-21] Spin polarization is considered. A plane wave basis set for electron wave functions with cutoff energy of 450 eV is used. Integrations in the Brillouin zone are performed using a 13x5x15 k-grid generated according to the Monkhorst-Pack scheme.[22] Structures are relaxed using a conjugate-gradient algorithm until the atomic forces are less than 0.02 eV/Å. Bader charges were calculated using the approach described in references.[23-26]

3. RESULTS AND DISCUSSION

3.1 Crystal structure. The crystal structure of the single crystal isolated by the tin flux growing method was studied using single crystal X-ray diffraction at room temperature. The crystallographic data for the single crystal are summarized in Table 1. This compound crystallizes with a centered orthorhombic unit cell, with a = 5.5931(1) Å, b = 18.8017(5) Å and c = 6.7005(2) Å. In addition, inspection of the systematic extinctions revealed that hkl (h+k≠2n), h0l (l≠2n) and hk0 (h≠2n) were not present, which is consistent with the space group Cmce (No.64). The positions of the five independent atoms, Sn(1) in (8f), Sn(2) in (8f), V(1) in (8e), V(2) in (8f) and Al(1) in (8e), were derived using direct methods. A series of refinements with the positional and anisotropic thermal parameters converged to the agreement factors R_1 = 2.86% and wR_2 = 8.48%. The final refinements including occupation factors for all atoms showed a mixed occupation at Sn sites with 0.966(1)/0.034(1) for Sn(1)/Al(1) and 0.848(1)/0.152(1) for Sn(2)/Al(2), hence leading to the final reliability factors R_1 = 1.45 % and wR_2 = 2.85%. No other mixed occupancy was observed. As shown in Table 1, further difference Fourier calculations did not reveal any significant residual electron density peaks. Consequently, the composition of the investigated crystal is $Al_{1.19(2)}V_2Sn_{1.81(2)}$. The positional parameters standardized using the program Structure Tidy[27] are listed in Table 2, the anisotropic thermal factors are gathered in Table 3 and the main interatomic distances in Table 4.

Table 1: Crystallographic data, data collection and structure refinement parameters.

Chemical formula	$Al_{1+x}V_2Sn_{2-x}$, x = 0.19(2)
Formula weight (g mol^{-1})	349.20
Wavelength (Å)	0.71073
Crystal size (µm)	10 x 20 x 60
System	Orthorhombic
Space group	Cmce
Unit cell dimensions (Å)	*a* = 5.5931(1) *b* = 18.8017(5) c = 6.7005(2)
Volume ($Å^3$)	704.62(34)
Z	8
Calculated density (g cm^{-3})	6.584
Absorption coeff. (mm^{-1})	17.861
F(000)	1216.9
θ range for data collection (deg)	2.17-51.63
Index ranges	$-12 < h < 12$ $-40 < k < 41$ $-14 < l < 14$
Collected, independent reflections	24764/2109
Coverage of the reciprocal sphere (%)	100
Goodness-of-fit	1.084
R indices I>2s(I)-1906 refl all	R(int) = 0.0351, R1 = 0.0145, wR2 = 0.0285 R1 = 0.0176, wR2 = 0.0294
Extinction coefficient	0.0024(1)
Number of parameters refined	32
$\Delta\rho$max, $\Delta\rho$min ($eÅ^{-3}$)	1.209/–0.980

Table 2: Atomic coordinates and isotropic displacement parameters

Atom	site	x/a	y/b	z/c	U_{eq} (Å)	Occupancy
Sn(1)/Al(1)	8f	0.0	0.22275(2)	0.08033(2)	0.00755(2)	0.966(1)/0.034(1)
Sn(2)/Al(2)	8f	0.0	0.10975(2)	0.42614(2)	0.00649(2)	0.848(1)/0.152(1)
V(1)	8e	1/4	0.34059(2)	1/4	0.00592(3)	1
V(2)	8f	0.0	0.07724(2)	0.03164(3)	0.00608(3)	1
Al(3)	8e	1/4	0.48258(2)	1/4	0.00777(6)	1

T**able 3:** Anisotropic atomic displacement parameters ($Å^2$) for the crystal studied

	U11	U22	U33	U23	U13	U12
Sn(1)/Al(1)	0.00812(3)	0.00612(3)	0.00840(3)	-0.00177(2)	0	0
Sn(2)/Al(2)	0.00605(3)	0.00824(3)	0.00528(3)	-0.00157(2)	0	0
V(1)	0.00703(7)	0.00532(6)	0.00540(6)	0	-0.00119(5)	0
V(2)	0.00566(6)	0.00633(6)	0.00624(7)	-0.00099(5)	0	0
Al(3)	0.00684(15)	0.00670(14)	0.00978(16)	0	0.00262(12)	0

T**able 4:** Main interatomic distances (Å)

Sn(1)/Al(1) – 1V(2) 2.7552(2)
2V(1) 2.85606(17)
2V(1) 2.87618(12)
1Sn(2)/Al(2) 3.1437(1)
2Sn(1)/Al(1) 3.16698(10)
Sn(2)/Al(2) – 1V(2) 2.7131(2)
2V(1) 2.74516(12)
2V(2) 2.87651(7)
2Al(3) 3.0108(4)
2Al(3) 3.1109(3)
V(1) – 1Al(3) 2.6697(5)
2Sn(2)/Al(2) 2.74515(12)
2V(1) 2.79655(5)
2V(2) 2.8112(2)
1Sn(1)/Al(1) 2.85605(17)
V(2) – 2Al(3) 2.6041(3)
2Al(3) 2.6950(3)
2V(1) 2.8113(2)
1Sn(2)/Al(2) 2.87652(7)
Al(3) – 2V(2) 2.6042(3)
2V(2) 2.6950(3)
2Al(3) 2.79655(5)
2Sn(2)/Al(2) 3.0107(4)
2Sn(2)/Al(2) 3.1117(5)

This structural determination reveals that $Al_{1+x}V_2Sn_{2-x}$ crystallizes with the same structure reported for $GaV_{2-x}Sn_{2-x}$.[28,29] For the latter, Sn as well as V deficiencies have been measured by EDX leading to a composition of $GaV_{1.67}Sn_{1.67}$. All sites of the $Al_{1+x}V_2Sn_{2-x}$ structure exhibit full occupancy. A similar conclusion was drawn for the binary Ti_2Sn_3 compound, also isotypic with the ternary compound GaV_2Sn_2.[30,31]

The crystal structure displayed in Fig. 1 can be considered as a layered structure along the longer *b* axis. The first layer is composed of AlV_5 pentagon clusters sharing a common edge and pointing in opposite directions due to a glide plane. The second layer is composed of Sn/Al atoms forming octahedra.

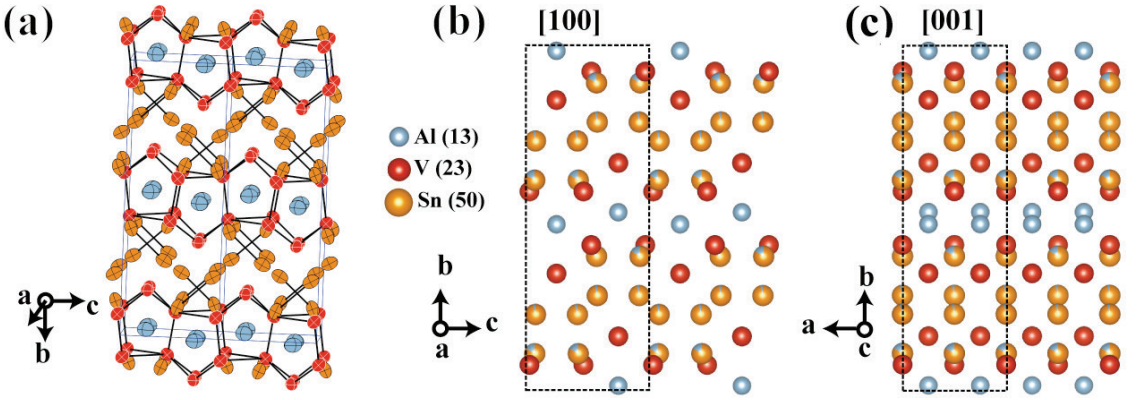

Figure 1: a) Representation by ellipsoids of the $Al_{1.19}V_2Sn_{1.81}$ crystal structure showing the AlV_5 pentagons and Sn/Al octahedra. The corresponding atomic hard sphere model with the mixed occupancies is viewed in b) along the [100] and in c) along the [001] projections. To understand the origin of the image contrasts observed in STEM, the atomic number for each element is given in brackets.

3.2 TEM analysis. Figure 2(a) shows a representative low magnification HAADF-STEM image (often referred to as *Z-contrast image*) of the $Al_{1.19}V_2Sn_{1.81}$ crystal viewed in the [100] zone-axis. The analysis of the corresponding experimental selected area electron diffraction (SAED) pattern, shown as an inset in Fig. 2(a), is in perfect agreement with the predicted crystal structure. Moreover, no apparent structural defects can be detected in the observed specimen regions.

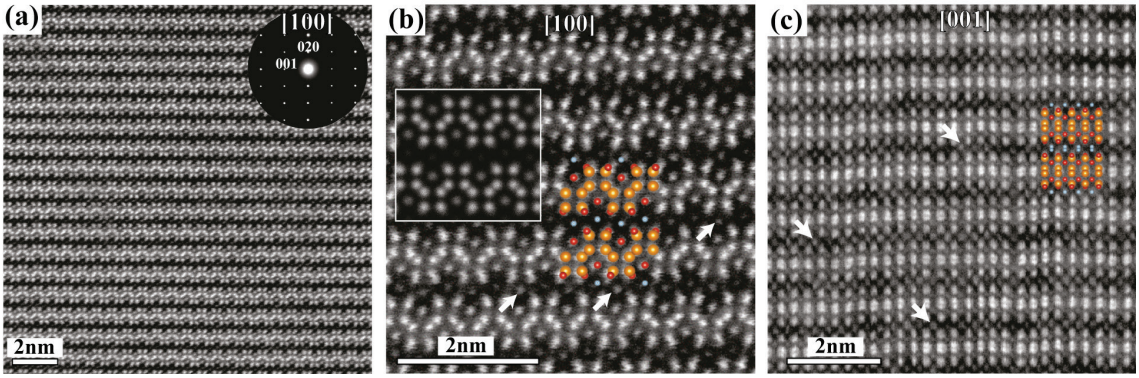

Figure 2: (a) Atomically resolved experimental unprocessed HAADF-STEM image with superimposed electron diffraction pattern of the Al-V-Sn compound and (b) High-resolution image with the superimposed calculated HAADF-STEM image based on predicted AlV_2Sn_2 atomic structure, both viewed in [100] zone axis. (c) High-resolution experimental HAADF-STEM image in [001] projection. Arrow marks indicate anomalously large intensities at the Al sites.

To resolve potential compositional variations over large specimen areas with high spatial resolution, an elemental EDX mapping procedure was applied. Typically, the elemental maps were acquired from rectangular regions to achieve analytical pixel resolution of 4 Å and with the total integration time, which would yield the counting error (σ) for major peaks (V-Kα line) around 1% relative. In addition to the three expected elements, i.e. Al, V and Sn, EDX analysis confirmed the presence of a small amount of Ga resulting from the FIB preparation. The average composition extracted from these elemental maps for Al, V, Sn and Ga was 17.4 at.%, 39.6 at.%, 41.8 at.% and 1.2 at.%, respectively. Within the given limits of the analytical spatial resolution, the EDX elemental maps indicate homogeneous distribution of all elements.

A representative high-magnification experimental atomic resolution HAADF-STEM images of the $Al_{1.19}V_2Sn_{1.81}$ ternary phase, viewed in the [100] and [001] zone-axis, are shown in Fig. 2(b,c), respectively. The contrast variation in the atomic-resolution Z-contrast images is roughly following the Z^2 dependence on the average atomic number of the probed atom column, which makes the reconstruction of both, atomic arrangements and atoms types of the underlying crystal structure relatively straightforward. The viewing projection of the low-magnification experimental HAADF

STEM image presented in Fig. 2(a) is to a first approximation described as a horizontal row structure with alternating contrast. The central regions of high-contrast rows are associated with the atomic columns fully occupied either by Sn or V atoms. The zig-zag structure of weaker intensity dots is found in-between the abovementioned bright rows. This is associated with atomic columns occupied by Al, which have the lowest atomic number (Z=13) amongst all three elements.

The experimental HAADF-STEM image of the top view, i.e. [001] zone-axis, of the same structure is as before represented by the alternative rows of bright and dark intensity, where bright rows are again occupied by the pure V and Sn atomic columns (Fig. 2(c)). In this projection, the Al columns are now represented as dumbbells of weak intensity in-between the bright-intensity rows. The corresponding $Al_{1.19}V_2Sn_{1.81}$ ternary phase structure, orientated in two viewing projections, which are superimposed on the experimental HAADF-STEM images show a perfect match between the image intensities and the projected atomic positions in the ternary phase structure.

A more detailed analysis of the image intensity of the HAADF-STEM images associated to individual atomic columns indicate that, in comparison to the Sn and V sites, the Al sites show non-periodic and anomalously large intensity variations for both, [100] and [001] zone axis (marked by arrows in Fig. 2(b,c)). To validate the experimentally observed intensity variations, detailed HAADF-STEM image calculations were performed from the predicted atomic model in [100], where Al atomic columns are separated enough to be clearly spatially resolved by STEM imaging. The resulting calculated HAADF-STEM image (inset in Fig. 2(b)), is well in accordance with the experimental image for the V and Sn sites. While there is a perfect match in the position for Al sites between the calculated and experimental HAADF-STEM image, the Al-sites intensity of the calculated image is typically lower and more uniform when compared with the experimental image. Such an anomalous intensity variation at the Al sites can be explained either by instrumental instabilities during image acquisition or as a unique property of the investigated crystal structure, which is related to partial substitution of Al sites with atoms of higher atomic number. In the latter case, the intensity variations between individual Al columns at exact positions should not change during subsequent image acquisition.

To further verify, what is the dominant mechanism for the above described anomalous intensity variation at the Al sites, a time-sequenced HAADF-STEM imaging was applied, where a series of images acquired from exactly the same specimen region were recorded with the time interval of 7 seconds, as shown in Fig. 3(a). These images were further aligned to compensate for instrumental drift during image acquisitions, by applying a post-processing image cross-correlation algorithm. The difference image between two aligned subsequent images is shown in Fig. 3(b). Several equivalent atomic column positions with anomalously large intensity are indicated by arrows. From this result it is evident that anomalous image intensity variations at the Al sites remain constant (no dynamics) during the acquisition of image series, which supports the idea that Al atoms are partially substituted with foreign atoms. A contrast variation could have also originated from atomic density differences between columns. However, this mechanism seems unlikely as Al sites have a full occupancy.

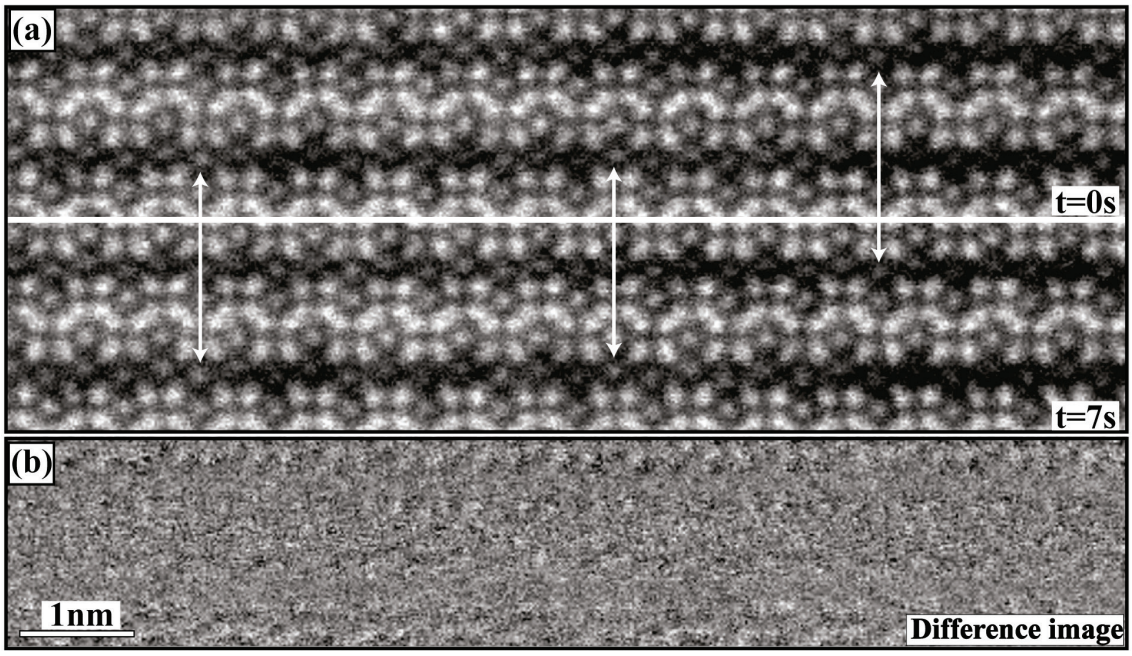

Figure 3: (a) A series of drift-corrected subsequently acquired images, Δt= 7s with the indicated equivalent atomic column positions (arrow marks). (b) Difference image confirms minimized drift image region.

3.3 Theoretical approach. *Ab initio* calculations have been performed using the ideal AlV_2Sn_2 structure with full single occupancies for all atoms. The cell parameters

resulting from the structural optimisation (a=5.62 Å, b=18.83 Å, c=6.73 Å) are in excellent agreement with the experimental ones (relative error smaller than 0.5%). There is also a good agreement between the calculated atomic positions and those deduced from XRD: the relative error is less than 2%, except for the z position of V(2) atoms. The results are gathered in Table 5.

Atom	site	x/a	y/b	z/c	Occupancy
Sn(1)	8f	0.0	0.223	0.078	1
Sn(2)	8f	0.0	0.110	0.424	1
V(1)	8e	1/4	0.343	1/4	1
V(2)	8f	0.0	0.076	0.026	1
Al	8e	1/4	0.483	1/4	1

Table 5: Calculated atomic positions in AlV_2Sn_2. For the calculations, no mixed occupancies have been considered at Sn sites.

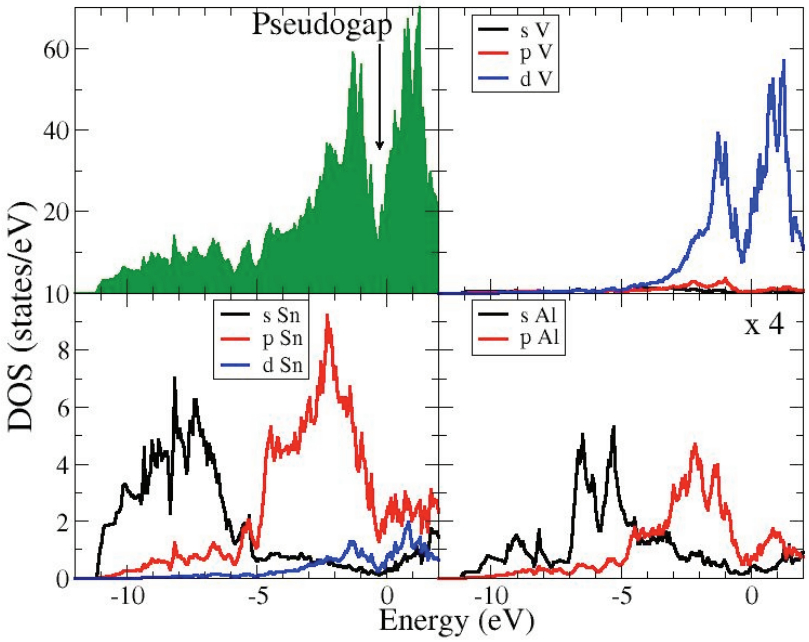

Figure 4: Density of States of the AlV_2Sn_2 compound. Upper left: total DOS with the pseudogap at the Fermi level highlighted by an arrow, upper right: *s*, *p* and *d* partial DOS for V, bottom left: *s*, *p* and *d* partial DOS for Sn, bottom right: *s* and *p* partial DOS for Al. The Fermi energy is set at the origin of the x-axis.

The calculated density of states (DOS) of the AlV_2Sn_2 compound is displayed in Fig. 4 together with Al *s,p*, V *s,p,d* and Sn *s,p,d* partial DOS. The metallic character of the compound is assessed from the many states present at the Fermi energy. The total DOS presents a marked *sp* character in the [-12,-6] eV region, which arises essentially from Sn atoms. Vanadium *d* states have a main contribution above -3 eV. A deep pseudogap, a reduction of the DOS near the Fermi energy, is found in the close vicinity of E_F. With an electron density of 2.51 e/at.[9] in an unit cell of volume 704.62 $Å^3$, one expects a diameter for the Fermi sphere equal to $2k_F$=3.2 $Å^{-1}$. The nearest reciprocal lattice vector with large intensities that could fulfil the pseudo-Brillouin zone - Fermi surface interaction lies at $2k_F$ = 3.0 $Å^{-1}$. It corresponds to the (260) planes. The presence of a pseudo-gap close to the Fermi level may then be attributed to both a Hume Rothery effect combined with strong *spd* hybridization.

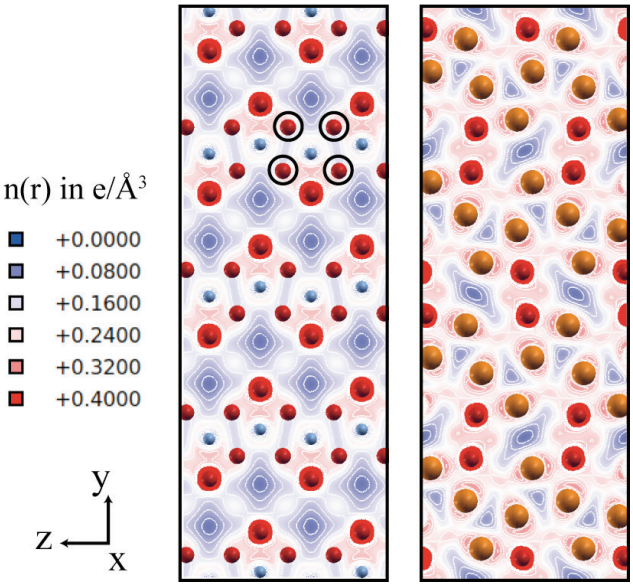

Figure 5: Charge distribution in the x=0.25 (left) and x≈0.5 (right) planes. The V atoms encircled sit slightly out of the figure plane. The Al, V and Sn atoms are represented as blue, red and orange spheres respectively.

Charge density calculations show that the charge distribution around *sp* metals is not spherical (Fig. 5). Charge accumulations are visible along the Al-V and Sn-V bonds. On the other hand, the Bader charge analysis shows that a charge transfer occurs from Al and V atoms that are both positively charged with on average +0.24 e/at. for Al atoms and +0.23 e/at. for V atoms towards Sn atoms exhibiting an average charge of -0.35

e/at, hence suggesting iono-covalent type bondings. These results are consistent with the respective electronegativities of the elements (1.63, 1.61 and 1.96 for V, Al and Sn, respectively, according to the Pauling scale).[32]

The $Al_{1+x}V_2Sn_{2-x}$ compound identified here is isostructural to the GaV_2Sn_2 phase. As explained above, the mutual replacement of Ga and Al can be considered as an isoelectronic substitution (same valence). To explore further this approach, the In-V-Sn system (In below Al and Ga in the Periodic Table) has been investigated and specifically near the InV_2Sn_2 region. Unfortunately, no ternary phases could be identified. Furthermore, to understand how modifying the number of valence electrons could affect the compound structure, a similar investigation has been carried out for the Si-V-Sn system. Once more, only the expected binary phases have been found during the phase characterisation. It has to be mentioned that contrary to Ga-V-Sn, the X-V-Sn (X= Al, In, Si) systems obey the PPA criteria, with In-V, Si-Sn and Al-Sn forming no defined compounds. While not identified throughout our systematic phase diagram exploration, the virtual InV_2Sn_2 and SiV_2Sn_2 compounds have been considered for further numerical experiments. The objective is to understand how different the electronic properties and charge distributions are across these structurally similar systems.

In fact, the electronic properties of the GaV_2Sn_2 compound, and the hypothetical InV_2Sn_2 and SiV_2Sn_2, are very similar to the ones of AlV_2Sn_2. Again, a deep pseudogap appears close to the Fermi energy. The position of the latter is similar for AlV_2Sn_2, InV_2Sn_2 and GaV_2Sn_2 (-0.33 eV, -0.35 eV and -0.39 eV, respectively), while it is shifted to higher bonding energies for SiV_2Sn_2 (-0.44 eV). In a rigid band model, this shift is expected as the replacement of Al by Si element leads to an additional valence electron in the system.

	AlV_2Sn_2	GaV_2Sn_2	InV_2Sn_2	SiV_2Sn_2
X	0.24	-0.30	-0.19	-0.48
Sn	-0.35	-0.28	-0.30	-0.23
V	0.23	0.43	0.39	0.47

Table 6: Bader charges calculated for XV_2Sn_2 compounds (X=Al, Ga, In, Si). The electronegativity values of the elements are 1.61 (Al), 1.63 (V), 1.78 (In), 1.81 (Ga), 1.90 (Si), and 1.96 (Sn).[32]

The main difference between AlV_2Sn_2 and XV_2Sn_2 (X=Ga, In, Si) compounds lies in the charge transfer (see Table 6). In the latter case, charge transfers occur from V atoms to both X and Sn atoms, which are both negatively charged. In the case of AlV_2Sn_2, charge transfers occur from V and Al to Sn atoms. These charge transfers are in agreement with the electronegativity values of the elements.[32]

Although the DOS at E_F and the charge transfer configuration are similar to those of the GaV_2Sn_2 compound, experimentally only binary compounds have been identified in the In-V-Sn system. The impossibility to grow a ternary compound, here the InV_2Sn_2 phase, could rely on other factors. For instance, the large atomic radius difference between In (1.55 Å) and Ga (1.30 Å) (and even Al (1.25 Å)) could lead to a compactness issue, prohibiting the formation of the phase. Regarding the Si-V-Sn situation, the instability of the phase may have an electronic origin. Indeed, the additional valence electron results in an energy shift of the pseudogap to higher energy and consequently to a greater DOS at E_F resulting from a partial filling of the steep anti-bonding states.

Up to now, only micrometre-size crystals of the AlV_2Sn_2 compound could be grown using conventional techniques. Further efforts will be devoted to increase the crystal size in order to perform transport measurements along specific crystallographic directions. The atypical GaV_2Sn_2 structure type has been initially described by two kinds of atoms bands.[28] Such transport measurements will reveal if the structure description is purely geometric or if it has any physical meaning. One may expect for instance associated anisotropic electrical and thermal properties as already reported for a different class of intermetallics.[33,34] Finally, it is foreseen from the TEM results that a $(Ga,Al)V_2Sn_2$ compound should exist. Indeed, the intensity variations at the Al sites, which do not change over time, could originate from a partial replacement of Al atoms by Ga element, which was supplied through the amorphized surface layer during the FIB specimen preparation. Consequently, these observations may encourage future works in that direction and in the exploration of the quaternary Ga-Al-V-Sn phase diagram.

CONCLUSIONS

The study of the Al-V-Sn phase diagram has been motivated by the Push-Pull alloy concept. Among the various samples elaborated, only one ternary phase has been identified up to now. It corresponds to the orthorhombic $Al_{1.19}V_2Sn_{1.81}$ compound which adopts the Cmce space group with the lattice parameters a = 5.5931(1) Å, b = 18.8017(5) Å and c = 6.7005(2) Å. The substitution of Al by Ga, regarded as an isoelectronic replacement, preserves the structure, as the $Al_{1.19}V_2Sn_{1.81}$ compound is isostructural to the GaV_2Sn_2 structure. This is not verified for In atoms although located in the same column of the Periodic Table as Al and Ga. The electronic structure of real and virtual XV_2Sn_2 (X=Ga, Al, In, Si) compounds show similar characteristics with a pseudogap around the Fermi level. There is a non-spherical charge distribution around the *sp* elements combined with charge accumulations along specific Al-V and Sn-V bonds. The charge transfers, which occur within the AlV_2Sn_2 structure, are in line with the respective element electronegativities. Finally, based on STEM observations and image simulations, we postulate on the existence of a $(Al,Ga)V_2Sn_2$ phase.

ACKNOWLEDGEMENT

In memory of our friends Dr. Esther Belin-Ferré and Prof. An-Pang Tsai.

EG acknowledges financial support through the COMETE project (COnception in silico de Matériaux pour l'EnvironnemenT et l'Energie) co-funded by the European Union under the program 'FEDER-FSE Lorraine et Massif des Vosges 2014-2020'. High Performance Computing resources were provided by GENCI under the allocation 99642, as well as the EXPLOR center hosted by the Université de Lorraine (allocation 2017M4XXX0108). JL acknowledges financial support from the Conseil Régional of Région Grand-Est. This work is a result of cooperation within the French-Slovene collaboration established under Push-Pull Alloys and Complex Compounds (PACS2) Joint Open Laboratory.

REFERENCES

[1] Dshemuchadse, J.; Steurer, W. More Statistics on Intermetallic Compounds – Ternary Phases. *Acta Cryst.* 2015, A71, 335-345.

[2] Dubois, J.-M.; Belin-Ferré, E.; Tsai, A. Quasicrystals and Complex Metallic Alloys; in *Kirk-Othmer Encyclopedia of Chemical Technology*. John Wiley & Sons, Inc., Hoboken, NJ, USA, 2016, 1-19.

[3] Krnel, M.; Vrtnik, S.; Koželj, P.; Kocjan, A.; Jagličić, Z.; Boulet, P.; de Weerd, M.C.; Dubois, J.M.; Dolinšek, J. Random-anisotropy ferromagnetic state in the $Cu_5Gd_{0.54}Ca_{0.42}$ intermetallic compound. *Phys. Rev. B: Condens. Matter Mater. Phys*. 2016, 93, 094202-13.

[4] Weber, T.; Dshemuchadse, J.; Kobas, M.; Conrad, M.; Harbrecht, B.; Steurer, W. Large, larger, largest - a family of cluster-based tantalum copper aluminides with giant unit cells. I. Structure solution and refinement. *Acta Cryst*. 2009, B65, 308-317.

[5] Kadok, J.; de Weerd, M.C.; Boulet, P.; Gaudry, É.; Grin, Y.; Fournée, V.; and Ledieu, J. Al_3AuIr: A New Compound in the Al−Au−Ir System. *Inorg. Chem*. 2015, 54, 7898-7905.

[6] Burkhardt, F.; Skela, B.; Daneu, N.; Samardzija, Z.; Sturm, S.; Gaudry, E.; Kobe, S.; Dubois, J.M.; A new complex ternary phase in the Al-Cr-Sc push-pull alloy, *J. Alloy. Comp.* 2018, 768, 230-239.

[7] Tsai, A.; Inoue, A.; Masumoto, T. New Stable Icosahedral Al-Cu-Ru and Al-Cu-Os Alloys. *Jpn. J. Appl. Phys*. 1988, 27, L1587-L1590.

[8] Guo, J.Q.; Tsai, A.P. Stable Icosahedral Quasicrystals in the Ag-In-Ca, Ag-In-Yb, Ag-In-Ca-Mg and Ag-In-Yb-Mg Systems. *Philos. Mag. Lett*. 2002, 82, 349-352.

[9] Mizutani, U.; Sato, H.; Inukai, M.; Nishino, Y.; Zijlstra, E. S. Electrons per Atom Ratio Determination and Hume-Rothery Electron Concentration Rule for P-based Polar Compounds Studied by FLAPW-Fourier calculations, *Inorg. Chem.* 2015, 54, 930−946.

[10] Tsai, A.-P. A test of Hume-Rothery rules for stable quasicrystals. *J. Non-Cryst*. 2004, 334 & 335, 317-322.

[11] Sheldrick, G.M. Structure Refinement with SHELXL. *Acta Cryst.* 2015, C71, 3.

[12] Veys, D.; Weisbecker, P.; Domenici, B.; Weber, S.; Fournée, V. ; Dubois, J.M. Chemical surface ageing in ambient conditions of an Al-Fe-Cr approximant phase, *J. Phys.: Cond. Matter*. 2007, 19, 376207.

[13] Koch, C. “Determination of Core Structure Periodicity and Density Along Dislocations,” PhD dissertation, Arizona State University (2002).

[14] Kresse, G.; Hafner, J. Ab Initio Molecular Dynamics for Liquid Metals. *Phys. Rev. B: Condens. Matter Mater. Phys*. 1993, 47, 558−561.

[15] Kresse, G.; Hafner, J. Ab Initio Molecular-Dynamics Simulation of the Liquid-Metal-Amorphous-Semiconductor Transition in Germanium. *Phys. Rev. B: Condens. Matter Mater. Phys.* 1994, 49, 14251−14269.

[16] Kresse, G.; Furthmüller, J. Efficiency of Ab-Initio Total Energy Calculations for Metals and Semiconductors Using a Plane Wave Basis Set. *Comput. Mater. Sci*. 1996, 6, 15-50.

[17] Kresse, G.; Furthmüller, J. Efficient Iterative Schemes for Ab Initio Total-Energy Calculations Using a Plane-Wave Basis Set. *Phys. Rev. B: Condens. Matter Mater. Phys*. 1996, 54, 11169-11186.

[18] Blöchl, P. E. Projector Augmented-Wave Method. *Phys. Rev. B: Condens. Matter Mater. Phys.* 1994, 50, 17953-17979.

[19] Kresse, G.; Joubert, D. From Ultrasoft Pseudopotentials to the Projector Augmented-Wave Method. *Phys. Rev. B: Condens. Matter Mater. Phys*. 1999, 59, 1758-1775.

[20] Perdew, J. P.; Burke, K.; Ernzerhof, M. Generalized Gradient Approximation Made Simple. *Phys. Rev. Lett*. 1996, 77, 3865-3868.

[21] Perdew, J. P.; Burke, K.; Ernzerhof, M. Erratum: Generalized Gradient Approximation Made Simple. *Phys. Rev. Lett*. 1997, 78, 1396.

[22] Monkhorst, H. J.; Pack, J. D. Special points for Brillouin-zone integrations. *Phys. Rev. B: Condens. Matter Mater. Phys*. 1976, 13, 5188-5192.

[23] Tang, W.; Sanville, E.; Henkelman, G. A grid-based Bader analysis algorithm without lattice bias, *J. Phys.: Condens. Matter* 2009, 21, 084204-7.

[24] Sanville, E.; Kenny, S. D.; Smith, R.; Henkelman, G. An Improved Grid-Based Algorithm for Bader Charge Allocation, *J. Comp. Chem*. 2007, 28, 899-908.

[25] Henkelman, G.; Arnaldsson, A.; Jónsson, H. A Fast and Robust Algorithm for Bader Decomposition of Charge Density. *Comput. Mater. Sci*. 2006, 36, 254-360.

[26] Yu, M.; Trinkle, D. R. Accurate and Efficient Algorithm for Bader Charge Integration. *J. Chem. Phys*. 2011, 134, 064111-8.

[27] Parthé, E.; Cenzual, K.; Gladyshevskii, R. J. Standardization of crystal structure data as an aid to the classification of crystal structure types. *J. Alloys Comp*. 1993, 197, 291-301.

[28] Ye, J.; Horiuchi, H.; Shishido, T.; Fukuda, T. Structure of V_2Sn_2Ga. *Acta Cryst*. 1990, C46, 1195-1197.

[29] Ye, J.; Horiuchi, H.; Shishido, T.; Toyota, N.; Ukei, K.; Sasaki, T.; Fukuda, T. Growth and Characterization of Va-Sn-Ga (Va = Ta, Nb, V) Superconducting Compounds, *J. Cryst. Growth* 1990, 99, 969-974.

[30] Künnen, B.; Jeitschko, W.; Kotzyba, G.; Mosel B.D. Crystal Structure and Properties of the Titanium Stannide Ti_2Sn_3, *Z. Naturforsch*. 2000, B 55, 425-430.

[31] Kleinke, H.; Waldeck, M.; Gütlich, P. Ti_2Sn_3: A Novel Binary Intermetallic Phase, Prepared by Chemical Transport at Intermediate Temperature, *Chem. Mater.* 2000, 12, 2219-2224.

[32] Electronegativity. In *Handbook of Chemistry and Physics 97th Edition*, Haynes, W.M., Ed.; CRC Press Taylor & Francis group, Boca Raton, 2017; Chapter 9, pp. 9-103.
http://www.softouch.on.ca/kb/data/CRC%20Handbook%20of%20Chemistry%20and%20Physics%20-%2097th%20Edition%20(2016).pdf

[33] Ivkov, J.; Popcevic, P.; Dolinšek, J.; Gille, P. Hall Effect of the $Al_{13}Fe_4$ Decagonal Approximant and Its Ternary Extension $Al_{13}(Fe,Ni)_4$. *Croat. Chem. Acta* 2010, 83, 107-111.

[34] Dolinšek, J.; Komelj, M.; Jeglič, P.; Vrtnik, S.; Stanic, D.; Popčevic, P.; Ivkov, J.; Smontara, A.; Jagličic, Z.; Gille, P.; Grin, Yu. Anisotropic Magnetic and Transport Properties of Orthorhombic $Al_{13}Co_4$. *Phys. Rev. B: Condens. Matter Mater. Phys*. 2009, 79, 184201-11.

For Table of Contents Only

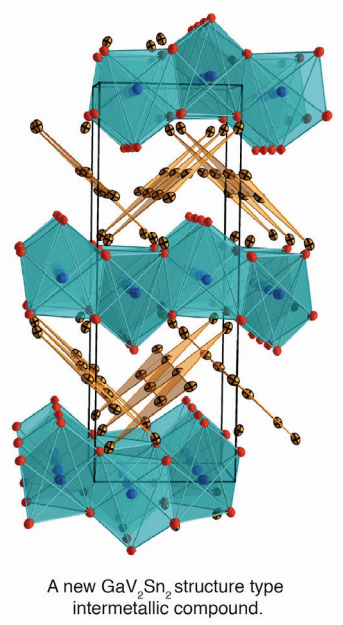

A new GaV_2Sn_2 structure type intermetallic compound.